14

Optical Properties of Quantum-Confined Semiconductor Structures Driven by Strong Terahertz Fields

Tong-Yi Zhang and Wei Zhao
State Key Laboratory of Transient Optics and Photonics, Xi'an Institute of Optics and Precision Mechanics, Chinese Academy of Sciences
People's Republic of China

1. Introduction

The development of femtosecond pulse lasers is one of the key breakthroughs in the field of terahertz (THz) technology. THz radiation (also called T-rays) lies in the frequency gap between the infrared and microwaves, loosely referred to the frequencies from 300 GHz to 30 THz. THz radiation has long been used in astronomy and analytical science. Despite great scientific interest, however, the THz frequency range remains one of the least developed regions of the electromagnetic spectrum, due to relative lack of convenient radiation sources, detectors and transmission technology. Thanks to the development of femtosecond pulse lasers, THz research has come into the center stage during the last quarter century. Most milestones in the development of THz technology, such as THz time-domain spectroscopy and THz pulse imaging, rely on the generation of THz pulse by employing high-power femtosecond laser pulse.

In parallel to the development of THz pulsed sources, there has been a rapid expansion in developing continuous or quasi-continuous THz wave sources, such as THz free-electron lasers, photomixers, and quantum cascade lasers. High-power and frequency-tunable THz free-electron lasers have been successfully applied in scientific research into optical and transport properties in different semiconductor structures. The strong THz ac fields can coherently modify the optical properties of semiconductors. This modulation of optical properties is an essential ingredient for advanced optoelectronic devices.

This chapter reviews two topics about THz radiation and is organized as follows. In section 2, the generation of THz pulses by exploiting femtosecond laser pulses to excite photoconductive antennas, nonlinear optical crystals, and quantum-confined structures is introduced, with emphasis on the large-aperture photoconductive antennas. In section 3, the fundamental theory about optical absorption and formulations of semiconductor Bloch equations (SBEs) are presented, which have been used to investigate the optical response of semiconductor structures pumped by intense THz radiation and probed by an infrared pulse. The modulated optical properties in quantum-confined semiconductor structures driven by strong THz fields are discussed in section 4. Finally, a brief summary is given in the last section. The contents of the chapter are based on the work by the authors' research group at Xi'an Institute of Optics and Precision Mechanics, Chinese Academy of Sciences, but some

relevant results of other groups are also introduced. We apologize to those whose work were not mentioned owing to space limitations.

2. THz pulse generation with ultrashort laser pulses

Two well-developed techniques of THz pulse generation are based on photoconductive antennas and optical rectification, which are the backbone of THz time-domain spectroscopy and THz pulse imaging. They rely on the excitation of different materials with ultrashort laser pulses. Quantum-confined semiconductor structures, as well as bulk semiconductors and semiconductor surfaces, emit transient THz radiation when excited with femtosecond laser pulses. And it has been developed into a new THz emission spectroscopic technique, which has been effectively used to investigate the coherent dynamics of a variety of materials and structures. In this section, THz pulse generation from photoconductive antennas, optical rectification, and quantum-confined structures is briefly introduced. The discussion is concerned principally with large-aperture photoconductive antennas because of their relative simplicity, both in fabrication and analysis, and their capabilities for high-power THz generation. A simple but unified description of their behavior is presented and the principal characteristics of these large-aperture photoconductive antennas are discussed.

2.1 Photoconductive antennas

A standard THz pulse generation scheme of photoconductive antenna is shown in Fig. 1. (Sakai & Tani, 2005) A photoconductive antenna consists of a coplanar transmission line and a dipole antenna with a small gap at the center. It is fabricated on a photoconductive substrate with short carrier lifetime, high mobility and high breakdown voltage, such as low temperature grown GaAs. A dc voltage is applied to the antenna, which generate an electric field in the semiconductor. The photoconductive gap is illuminated with femtosecond laser pulses (with photon energy greater than the bandgap of the material) to create electron-hole pairs. The free carriers accelerate in the bias field and form a short pulsed photocurrent, which radiate a transient electromagnetic pulse into free space. The photoconductive antenna behaves as a Hertzian dipole. Thus the radiated electric field $E(r,t)$ at a distance r (much greater than the wavelength of the radiation) and time t is described by the dipole antenna radiation formula

$$E\left(r,t\right)=\frac{l_e}{4\pi\varepsilon_0 c^2 r}\frac{\partial J\left(t\right)}{\partial t}\sin\theta, \tag{1}$$

where $J(t)$ is the current in the dipole, l_e is the effective length of the dipole, ε_0 is the dielectric constant of a vacuum, c is the velocity of light in a vacuum, and θ is the angle from the direction of the dipole. This source operates with comparatively low power, but the beam is stable and coherent with well known temporal characteristics. Hence it is commonly used for spectroscopy and imaging with high spectral resolution and excellent signal-to-noise ratio.

In order to generate high-power and wide beam THz pulse, large-aperture photoconductive antenna biased with a high dc voltage is used by pumping them with amplified femtosecond laser pulses. These photoconductive emitters are capable of relatively large average THz powers of 40 μW and bandwidths as high as 4 THz. Large-aperture photoconductive antenna are defined to have an optically illuminated area of dimensions much greater than the center wavelength of the emitted THz radiation. The characteristics of large-aperture

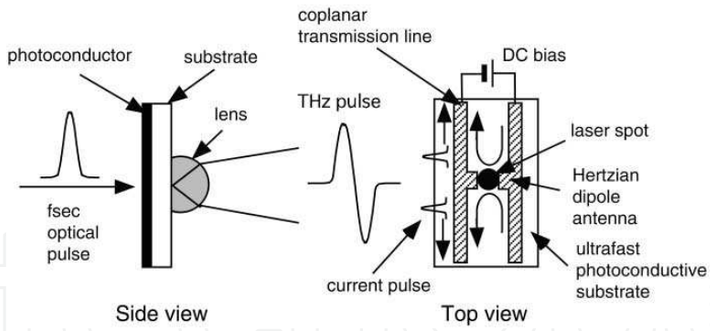

Fig. 1. Standard THz-pulse generation from a photoconductive antenna pumped with a femtosecond optical pulse. Propagation of current pulses along the coplanar transmission line are shown in the top view. (Sakai & Tani, 2005)

photoconductive antenna are well described by the current surge model. (Darrow et al., 1992; Zhang & Cao, 2004)

The current surge model assumes that THz electromagnetic field is radiated by a transient current generated at the surface of a photoconductive antenna. The surface current density $J_s(t)$ is determined by Ohm's law

$$J_s(t) = \sigma_s(t)\left[E_b + E_s(t)\right], \tag{2}$$

where $\sigma_s(t)$ is the time-dependent surface conductivity, E_b is the bias field, and $E_s(t)$ is the generated radiation field at the antenna surface. From the boundary conditions of Maxwell's equations and the finite size of the large-aperture antenna, the generated radiation field at antenna surface is related to the surface current density as

$$E_s(t) = -\frac{\eta_0}{1+\sqrt{\varepsilon}} J_s(t), \tag{3}$$

where $\eta_0 = 1/(\varepsilon_0 c) = 376.7\ \Omega$ is the impedance of free space and ε is the relative dielectric constant of the photoconductor. From Eq. (2) and Eq. (3), the radiation field at the antenna surface can be expressed through the bias field as

$$E_s(t) = -\frac{\eta_0 \sigma_s(t)}{\eta_0 \sigma_s(t) + \left(1+\sqrt{\varepsilon}\right)} E_b. \tag{4}$$

The surface current can be expressed through the applied electric field from Eq. (2) and Eq. (4) as

$$J_s(t) = -\frac{(1+\sqrt{\varepsilon})\sigma_s(t)}{\eta_0 \sigma_s(t) + (1+\sqrt{\varepsilon})} E_b. \tag{5}$$

The transient current at the antenna surface will radiate electromagnetic radiation. From Maxwell's equations, in the Coulomb gauge, the radiation field is given by

$$E_{rad}(r,t) = -\frac{1}{4\pi\varepsilon_0 c^2}\frac{\partial}{\partial t}\int \frac{J_s\left(r', t - |r-r'|/c\right)}{|r-r'|} ds', \tag{6}$$

where the surface current J_s in the emitting antenna is evaluated at a retarded time, r is the displacement from the antenna center, ds' is the increments of surface area at a displacement

r' from the antenna center, and the integration is taken over the surface of the illuminated region of the antenna. Eq. (6) shows that the far field is proportional to the time derivative of the surface current density. As a first order approximation, we substitute the integration by multiplying the area of the radiating surface to the surface current density. Thus the radiated field at far field is given by

$$E_{far}(t) = \frac{A}{4\pi\varepsilon_0 c^2 z} \frac{\left(1+\sqrt{\varepsilon}\right)^2 \dot{\sigma}_s(t-z/c)}{\left[\eta_0 \sigma_s(t-z/c)+\left(1+\sqrt{\varepsilon}\right)\right]^2}, \tag{7}$$

where A is the effective emitting area, z is the distance of observation point away from the center of the area, and the dot above the $\sigma_s(t)$ implies differential respective to time.
The surface conductivity induced by an optical beam of intensity $I_{opt}(t)$ is a convolution of $I_{opt}(t)$ with time-dependent mobility $\mu(t)$ and the carriers decay

$$\sigma_s(t) = \frac{q(1-R)}{h\upsilon} \int_{-\infty}^{t} \mu(t-t') I_{opt}(t') \exp\left(-\frac{t-t'}{\tau_c}\right) dt', \tag{8}$$

where q is the elementary charge, R is the optical reflectivity of the illuminated surface, $h\upsilon$ is the photon energy, τ_c is the lifetime of carriers. From the equation of motion of an electron in a electric field

$$\frac{dv(t)}{dt} = \frac{qE}{m^*} - \frac{v(t)}{\tau_s}, \tag{9}$$

and with the definition of mobility we obtain the time-dependent mobility

$$\mu(t) = \frac{q\tau_s}{m^*}\left[1-\exp\left(-\frac{t}{\tau_s}\right)\right] = \mu_s\left[1-\exp\left(-\frac{t}{\tau_s}\right)\right], \tag{10}$$

where m^* is the effective mass of electrons in the photoconductor, τ_s is the relaxation time, and $\mu_s = q\tau_s/m^*$ is the static mobility. To analyze the effect of exciting optical pulse, we assume the pump pulse has a Gauss temporal profile as

$$I_{opt}(t) = \frac{F}{2\sqrt{\pi}\Delta t} \exp\left(-\frac{t^2}{\Delta t^2}\right), \tag{11}$$

where F is the total pump optical fluence, and $\sqrt{\ln 2}\Delta t$ is the full width at half maximum (FWHM) of the optical pulse. By inserting Eq. (10) and Eq. (11) into Eq. (8), we can deduce the time-dependent surface conductivity and its time differential as

$$\begin{aligned}\sigma_s(t) = \frac{q^2\tau_s}{m^*}\frac{(1-R)F}{4h\upsilon}\Bigg\{&\exp\left(-\frac{t}{\tau_c}\right)\exp\left(\frac{\Delta t}{2\tau_c}\right)^2\left[1+\operatorname{erf}\left(\frac{t}{\Delta t}-\frac{\Delta t}{2\tau_c}\right)\right]\\ &-\exp\left(-t\left(\frac{1}{\tau_c}+\frac{1}{\tau_s}\right)\right)\exp\left(\frac{\Delta t}{2}\left(\frac{1}{\tau_c}+\frac{1}{\tau_s}\right)\right)^2\\ &\times\left[1+\operatorname{erf}\left(\frac{t}{\Delta t}-\frac{\Delta t}{2}\left(\frac{1}{\tau_c}+\frac{1}{\tau_s}\right)\right)\right]\Bigg\},\end{aligned} \tag{12}$$

and

$$\dot{\sigma}_s(t) = \frac{q^2\tau_s}{m^*}\frac{(1-R)F}{4h\nu}\left\{\left(\frac{1}{\tau_c}+\frac{1}{\tau_s}\right)\exp\left(-t\left(\frac{1}{\tau_c}+\frac{1}{\tau_s}\right)\right)\exp\left(\frac{\Delta t}{2}\left(\frac{1}{\tau_c}+\frac{1}{\tau_s}\right)\right)^2\right.$$
$$\times\left[1+\mathrm{erf}\left(\frac{t}{\Delta t}-\frac{\Delta t}{2}\left(\frac{1}{\tau_c}+\frac{1}{\tau_s}\right)\right)\right]$$
$$\left.-\frac{1}{\tau_c}\exp\left(-\frac{t}{\tau_c}\right)\exp\left(\frac{\Delta t}{2\tau_c}\right)^2\left[1+\mathrm{erf}\left(\frac{t}{\Delta t}-\frac{\Delta t}{2\tau_c}\right)\right]\right\}. \tag{13}$$

Substituting Eq. (12) into Eq. (4), and Eq. (13) into Eq. (7), we obtain the explicit expressions for the surface field and the far field. The second term in the brace bracket in Eq. (12) and the first term in the brace bracket in Eq. (13) contain the effect of transient carrier mobility on the waveforms of the surface and radiated fields. The error function is the result of the convolution of optical intensity and the exponential decay. It reflects the two competing processes of carrier accumulating by photo-generation and carrier decaying by recombination. By defining a saturation fluence F_{sat}

$$F_{sat} = \frac{4h\nu(1+\sqrt{\varepsilon})}{q\mu_s\eta_0(1-R)}, \tag{14}$$

and denoting the parts in brace bracket in Eq. (12) and Eq. (13) as $\Sigma_1(t)$ and $\Sigma_2(t)$ respectively, we can express radiation field at surface and at far field in more compact forms, which the saturation property of the surface field at large F/F_{sat} is more obvious,

$$E_s(t) = -\frac{\frac{F}{F_{sat}}\Sigma_1(t)}{1+\frac{F}{F_{sat}}\Sigma_1(t)}E_b, \tag{15}$$

and

$$E_{far}(t) = \frac{A(1+\sqrt{\varepsilon})}{4\pi c}\frac{\frac{F}{F_{sat}}\Sigma_2(t-z/c)}{z\left[1+\frac{F}{F_{sat}}\Sigma_1(t-z/c)\right]^2}E_b. \tag{16}$$

Figure 2 shows the temporal shapes of the surface field and far field at different pumping fluence calculated by Eq. (15) and by Eq. (16), respectively. The normalized fluence F/F_{sat} varies from 1 to 10 at step 1. And the following typical values: $\tau_c = 1$ ps, $\tau_s = 0.5$ ps, $\Delta t = 0.1$ ps, are used. And the distance z is equal to 1 cm. It shows that the risetimes of the surface fields are about 500 fs. It indicates that the risetime of the surface field is determined by the carrier relaxation time. This is because it takes up a little time for the transient mobility to reach its quasi-equilibrium value. As the saturation property shown in Eq. (15), the spacing between the amplitudes of the surface fields is reducing as F/F_{sat} increases. With the fluence increasing, the peak of the radiation field increases and tend to saturation, the peak arrives earlier in time, the risetime of the main pulse decreases, and the pulse width decreases also.
Figure 3 shows the influence of the relaxation time and the carrier lifetime on the amplitudes and the pulse width of the radiated far field at different pumping fluence, respectively. Longer relaxation time results in a smaller amplitude value. This is due to the carriers reach their static mobility more slowly, thus the average velocity or the conductivity is low. Longer lifetime of the carriers results in a slight larger amplitude of the radiation field. This is due to more

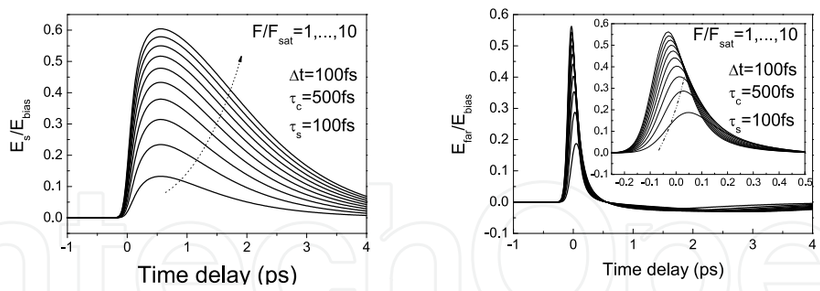

Fig. 2. Temporal shapes of the surface field (a) and far field (b) at different fluence, with the main pulses shown in the inset of (b). (Zhang & Cao, 2004)

accumulation of carriers and a larger current generated in the surface. But the influence of carrier lifetime is less prominent than the influence of relaxation time. The influence of the relaxation time on the pulse width of the radiated far field is much more prominent than the influence of the carrier lifetime. In the strong saturation regime ($F/F_{sat} = 10$), the influence of the relaxation time is reverse to that in the moderate saturation or in under-saturation regime ($F/F_{sat} = 1$ and $F/F_{sat} = 0.1$). The influence of the carrier lifetime on the pulse width is not monotonous. There are some fluctuations depended on the optical fluence.

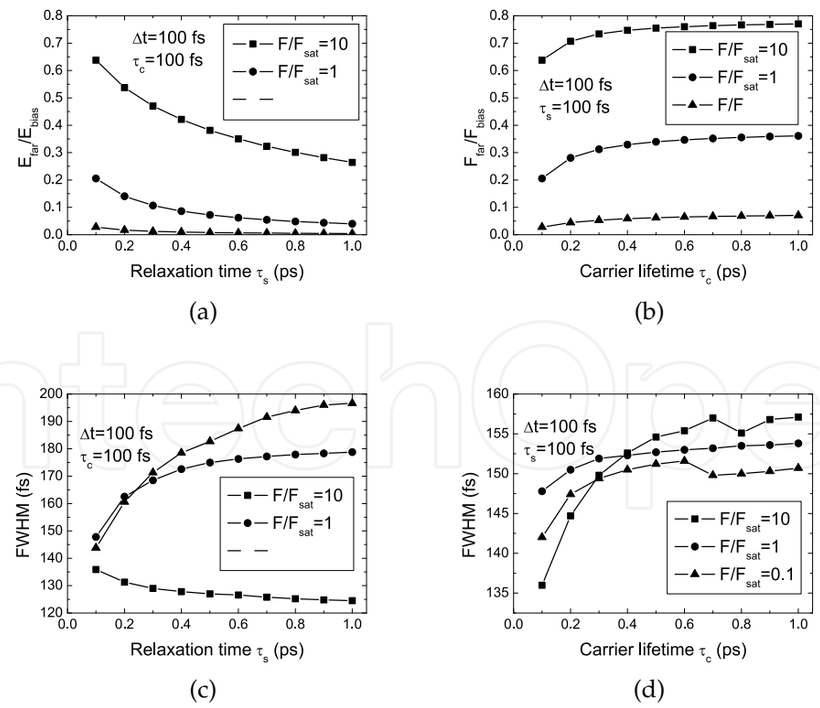

Fig. 3. Influence of the relaxation time and the carrier lifetime on the amplitudes (a) and (b), and on the pulse width (c) and (d) of the radiated far field at different pumping optical fluence. (Zhang & Cao, 2004)

2.2 Optical rectification

In optical rectification, the second-order nonlinear optical properties of materials excited by ultrafast laser pulses are used. These nonlinear effects arise when one illuminates a nonlinear optical crystal with high intensity laser. The ultrashort optical pulses contain various spectral components and the beatings between the different frequency components contained in a single ultrashort pulse will generate a broadband THz pulses. The nonlinear polarization created by a single optical pulse with the complex amplitude of the electric field $\mathcal{E}$ is given by

$$P(\omega) = \varepsilon_0 \chi^{(2)} \int_{-\infty}^{+\infty} \mathcal{E}_{opt}(\omega') \mathcal{E}_{opt}^{*}(\omega - \omega') d\omega', \tag{17}$$

where $\chi^{(2)}$ is the second-order susceptibility. The Fourier transformation of this equation gives second-order nonlinear polarization in the time domain

$$P(t) = \varepsilon_0 \chi^{(2)} \mathcal{E}_{opt}(t) \mathcal{E}_{opt}^{*}(t) \propto I_{opt}(t). \tag{18}$$

The first-order time derivative of this second-order nonlinear polarization gives the time-dependent current, thus the radiated THz field is proportional to the second-order time derivative of this nonlinear polarization. In this case, the optical beam itself is the origin of THz radiation, thus this process provides THz radiation only with very low efficiency, but has the advantage of very high bandwidths. Frequencies up to 41 THz have been accomplished. (Huber et al., 2000)

2.3 Quantum-confined semiconductor structures.

When pulsed lasers are used to excite coherently two energy levels in quantum well systems, beating phenomena can be observed. The beats involving spatial charge oscillations will emit electromagnetic radiation at the beat frequency. THz radiation emitted from a double coupled quantum well (Roskos et al., 1992) and a single quantum well (Planken et al., 1992) after optical excitation were observed. In the former, a coherent superposition of the symmetric and antisymmetric eigenstates of the coupled wells leads to the coherent tunneling of electrons between the two wells and therefore to a time-varying dipole moment. In the latter, a coherent superposition of the heavy hole (hh) and light hole (lh) excitons leads to charge oscillations in the well at the lh-hh splitting frequency. Both the oscillating charge emitted THz radiation into free space.

When quantum wells are embedded in a planar wavelength-scale optical microcavity, the light-matter interactions are largely modified owing to the confinement of the light field. In the strong coupling regime, hybrid exciton-photon modes (known as cavity polaritons) are formed. An excitation of such a system by a short laser pulse can trigger a complementary oscillation in the exciton and photon populations. The oscillation, called normal mode oscillation (NMO), corresponds to the intuitive time-domain picture of polaritons, where the energy is exchanged periodically between the excitons and photons. In GaAs-based semiconductor microcavities, the frequency of NMO lies in the THz regime. Then THz radiation is emitted from cavity-polaritons undergoing NMO.

For dc biased superlattices, resonant excitation of the lowest exciton connected to the optical transition between the first electron and hole miniband, electron-hole pairs are optically created in the miniband. The carriers perform "Bloch oscillation" both in real-space and momentum-space and emits THz radiation into free space. The Bloch frequency $\omega_B = eFd/\hbar$,

where e is the elementary charge, $\hbar$ is the reduced Planck constant, F is the applied DC electric field, d is the period of the superlattice. Ultrafast experiments on high-quality samples unambiguously demonstrated that electrons in superlattice minibands perform at least a few cycle Bloch oscillations.

3. Formulation for theoretical analysis

The optical absorption coefficient $\alpha(\omega)$ of a dielectric medium is related to the optical dielectric function $\varepsilon(\omega)$ by

$$\alpha(\omega) = \frac{\omega}{n(\omega)c}\varepsilon''(\omega), \tag{19}$$

where $n(\omega) = \sqrt{\frac{1}{2}\left[\varepsilon'(\omega) + \sqrt{\varepsilon'^2(\omega) + \varepsilon''^2(\omega)}\right]}$ is the index of refraction, $\varepsilon'(\omega)$ and $\varepsilon''(\omega)$ are the real and imaginary parts of $\varepsilon(\omega)$, respectively. The optical dielectric function is related to the optical susceptibility $\chi(\omega)$ via $\varepsilon(\omega) = 1 + \chi(\omega)$. While the optical susceptibility relates the excitation optical field $\mathcal{E}(t)$ with its induced macroscopic polarization $P(t)$ in time-domain via

$$P(t) = \varepsilon_0 \int_{-\infty}^{t} dt' \chi(t;t')\mathcal{E}(t'). \tag{20}$$

For a system in equilibrium, the optical susceptibility depends only on the time difference. By performing a Fourier transform of eq.(20) with the time difference, $\chi(\omega)$ can be obtained from

$$\chi(\omega) = \frac{\tilde{P}(\omega)}{\varepsilon_0 \tilde{\mathcal{E}}(\omega)}, \tag{21}$$

where $\tilde{\mathcal{E}}(\omega)$ and $\tilde{P}(\omega)$ are the Fourier transform of the optical field $\mathcal{E}(t)$ and the polarization function $P(t)$. To obtain the macroscopic polarization, we use the powerful semiconductor Bloch equations (SBEs).

3.1 Semiconductor Bloch Equations and their extension in *k*-space

The SBEs are a set of coupled differential equations, which governs the coupled dynamics of electrons, holes and the optical polarization in the spectral vicinity of the semiconductor bandgap. They are the direct generalization of the equations for the free-carrier transitions, which can be put into the form of Bloch equations, and have become the standard model for semiconductor optics. The SBEs are of considerable complexity in derivation, and the detailed derivation can be found in Haug and Koch's textbook (Haug & Koch, 2004). They describes consistently the phenomena, such as, proper dependence on the light field, the inclusion of the valence conduction band continuum states, exciton effects, as well as band-filling dynamics. It successfully covers linear as well as nonlinear phenomena, such as pump-probe, four-wave-mixing, or photon echo experiments.

In k-space, the macroscopic interband polarization $\mathbf{P}(t)$ is the sum of the microscopic interband polarization $\mathbf{p_k}$, $\mathbf{P}(t) = 2d_{cv}\sum_{\mathbf{k}} \mathbf{p_k}(t)$, where d_{cv} is the interband dipole matrix element and the factor 2 is due to the spin degeneracy. In the two-band model, the microscopic interband polarization is defined as $\mathbf{p_k}(t) = \langle \beta_{-\mathbf{k}}\alpha_{\mathbf{k}} \rangle$, where $\alpha_{\mathbf{k}}$ ($\beta_{-\mathbf{k}}$) is the annihilation operator of an electron (a hole) with wavevector $\mathbf{k}$ ($-\mathbf{k}$) in the conduction (valence) band. Under Hartree-Fock approximation, from the Heisenberg equations of motion for the electron and hole operators, the well-known SBEs for microscopic polarization $p_{\mathbf{k}}(t)$ and carrier

population $n^e_{\mathbf{k}} = \langle \alpha^\dagger_{\mathbf{k}} \alpha_{\kappa} \rangle$ and $n^h_{\mathbf{k}} = \left\langle \beta^\dagger_{-\mathbf{k}} \beta_{-\mathbf{k}} \right\rangle$ can be derived as

$$\frac{\partial}{\partial t} p_{\mathbf{k}} = -\frac{i}{\hbar} \left(\epsilon^e_{\mathbf{k}} + \epsilon^h_{\mathbf{k}} \right) p_{\mathbf{k}} + i \left(1 - n^e_{\mathbf{k}} - n^h_{\mathbf{k}} \right) \Omega_{R,\mathbf{k}} + \frac{\partial}{\partial t} p_{\mathbf{k}} |_{scatt}, \tag{22}$$

$$\frac{\partial}{\partial t} n^e_{\mathbf{k}} = -2 \, \mathrm{Im} \left[\Omega_{R,\mathbf{k}} p^*_{\mathbf{k}} \right] + \frac{\partial}{\partial t} n^e_{\mathbf{k}} |_{scatt}, \tag{23}$$

$$\frac{\partial}{\partial t} n^h_{\mathbf{k}} = -2 \, \mathrm{Im} \left[\Omega_{R,\mathbf{k}} p^*_{\mathbf{k}} \right] + \frac{\partial}{\partial t} n^h_{\mathbf{k}} |_{scatt}, \tag{24}$$

where $\epsilon^\lambda_{\mathbf{k}} = (E^\lambda_{\mathbf{k}} - \sum_{\mathbf{q}} V_{|\mathbf{k}-\mathbf{q}|} n^\lambda_{\mathbf{q}})/\hbar$ are the electron and hole energies renormalised by Coulomb interactions, $E^{(e,h)}_{\mathbf{k}}$ are the electron and hole band dispersions, $\Omega_{R,\mathbf{k}} = (d_{cv}\mathcal{E}(t) + \sum_{\mathbf{q}\neq\mathbf{k}} V_{|\mathbf{k}-\mathbf{q}|} p_{\mathbf{q}})/\hbar$ is the generalized Rabi frequency, $V_{\mathbf{q}}$ is the Fourier transform of Coulomb potential. The scattering terms represent the higher-order Coulomb correlations between carriers and carrier-phonon collisions.

In the presence of a driving field $\mathbf{F}$, the two-band SBEs are extended to the following forms (Meier et al., 1994; 1995; Zhang et al., 2007)

$$\frac{\partial}{\partial t} p_{\mathbf{k}} = -\frac{i}{\hbar} \left(\epsilon^e_{\mathbf{k}} + \epsilon^h_{\mathbf{k}} \right) p_{\mathbf{k}} + i \left(n^e_{\mathbf{k}} + n^h_{\mathbf{k}} - 1 \right) \Omega_{R,\mathbf{k}} - \frac{e}{\hbar} \mathbf{F} \cdot \nabla_{\mathbf{k}} p_{\mathbf{k}} + \frac{\partial}{\partial t} p_{\mathbf{k}} |_{scatt}, \tag{25}$$

$$\frac{\partial}{\partial t} n^e_{\mathbf{k}} = -2 \, \mathrm{Im} \left[\Omega_{R,\mathbf{k}} p^*_{\mathbf{k}} \right] - \frac{e}{\hbar} \mathbf{F} \cdot \nabla_{\mathbf{k}} n^e_{\mathbf{k}} + \frac{\partial}{\partial t} n^e_{\mathbf{k}} |_{scatt}, \tag{26}$$

$$\frac{\partial}{\partial t} n^h_{\mathbf{k}} = -2 \, \mathrm{Im} \left[\Omega_{R,\mathbf{k}} p^*_{\mathbf{k}} \right] - \frac{e}{\hbar} \mathbf{F} \cdot \nabla_{\mathbf{k}} n^h_{\mathbf{k}} + \frac{\partial}{\partial t} n^h_{\mathbf{k}} |_{scatt}. \tag{27}$$

In quantum-confined semiconductor structures, the two-band SBEs have to be generalized to a multiband description of anisotropic semiconductors, (Binder et al., 1994; Meier et al., 1995) as

$$\frac{\partial}{\partial t} p_{ji,\mathbf{k}} = -\frac{i}{\hbar} \sum_{i'j'} \left(\epsilon^e_{ii',\mathbf{k}} \delta_{jj'} + \epsilon^h_{jj',-\mathbf{k}} \delta_{ii'} \right) p_{j'i',\mathbf{k}} - \frac{i}{\hbar} \mathcal{U}_{ij,\mathbf{k}} \left(1 - n^e_{i,\mathbf{k}} - n^h_{j,\mathbf{k}} \right) - \frac{e\mathbf{F}}{\hbar} \cdot \nabla_{\mathbf{k}} p_{ji,\mathbf{k}} + \frac{\partial p_{ji,\mathbf{k}}}{\partial t} |_{scatt} \tag{28}$$

$$\frac{\partial}{\partial t} n^e_{i,\mathbf{k}} = -\frac{i}{\hbar} \sum_{j'} \left(\mathcal{U}_{ij',\mathbf{k}} p^*_{j'i,\mathbf{k}} - \mathcal{U}^*_{ij',\mathbf{k}} p_{j'i,\mathbf{k}} \right) - \frac{e\mathbf{F}}{\hbar} \cdot \nabla_{\mathbf{k}} n^e_{i,\mathbf{k}} + \frac{\partial n^e_{i,\mathbf{k}}}{\partial t} |_{scatt} \tag{29}$$

$$\frac{\partial}{\partial t} n^h_{j,-\mathbf{k}} = -\frac{i}{\hbar} \sum_{j'} \left(\mathcal{U}_{i'j,\mathbf{k}} p^*_{ji',\mathbf{k}} - \mathcal{U}^*_{i'j,\mathbf{k}} p_{ji',\mathbf{k}} \right) - \frac{e\mathbf{F}}{\hbar} \cdot \nabla_{\mathbf{k}} n^h_{j,-\mathbf{k}} + \frac{\partial n^h_{j,-\mathbf{k}}}{\partial t} |_{scatt} \tag{30}$$

with

$$\mathcal{U}_{ij,\mathbf{k}} = \mu_{ij,\mathbf{k}} \mathcal{E}(t) - \sum_{i'j',\mathbf{k}'} V \begin{pmatrix} \mathbf{k} & -\mathbf{k}' & -\mathbf{k}\mathbf{k}' \\ i & j' & j & i' \end{pmatrix} p_{j'i',\mathbf{k}}$$

$$\epsilon^e_{ii',\mathbf{k}} = E^e_{i,\mathbf{k}} \delta_{ii'} - \sum_{i'',\mathbf{k}''} V \begin{pmatrix} \mathbf{k}\mathbf{k}'' & \mathbf{k}\mathbf{k}'' \\ ii'' & i'i'' \end{pmatrix} n^e_{i'',\mathbf{k}''}$$

$$\epsilon^h_{jj',\mathbf{k}} = E^h_{j,\mathbf{k}} \delta_{jj'} - \sum_{j'',\mathbf{k}''} V \begin{pmatrix} \mathbf{k}\mathbf{k}'' & \mathbf{k}\mathbf{k}'' \\ j'j'' & jj'' \end{pmatrix} n^h_{j'',\mathbf{k}''}$$

where $E^{(e,h)}_{(i,j),\mathbf{k}}$ are the electron and hole band dispersions in subband i and j, respectively, $\epsilon^{e}_{ii',\mathbf{k}}$ and $\epsilon^{h}_{jj',\mathbf{k}}$ are the renormalized electron and hole band dispersions in subband i and j, respectively, $\mathcal{U}_{ij,\mathbf{k}}$ is the renormalized energies, $\mu_{ij,\mathbf{k}}$ is the optical dipole matrix element between conduction-band i and valence-band j states.

3.2 Semiconductor Bloch Equations in real-space

For some realistic one-dimensional structures, like V-groove and T-shaped quantum wires, it is very difficult to employ the SBEs in k-space to dealing the optical properties of these structures. This is due that the expansion in a problem-adapted basis leads to four-dimensional integrals for the Coulomb interaction, while an expansion in a basis where the Coulomb potential is not a problem will probably show a very slow convergence with basis size. For these structures, one has to take advantage of real-space method. The main idea is to solve directly a time-dependent inhomogeneousthe Schrödinger equation which describes the electron-hole dynamics in the presence of the Coulomb interaction, quantum confinements, and possible external magnetic and electric fields. The inhomogeneousthe Schrödinger equation takes the form of

$$i\hbar\frac{d\psi(\mathbf{r}_e,\mathbf{r}_h,t)}{dt} = \hat{H}\psi(\mathbf{r}_e,\mathbf{r}_h,t) - i\hbar\gamma\psi(\mathbf{r}_e,\mathbf{r}_h,t) - d_{cv}\delta(\mathbf{r}_e-\mathbf{r}_h)\mathcal{E}(t), \tag{31}$$

where $\psi(\mathbf{r}_e,\mathbf{r}_h,t)$ is the electron-hole-pair amplitude, $\hat{H}$ is the electron-hole Hamiltonian of the system considered, γ is a phenomenological dephasing constant. This equation can be considered essentially as SBEs in real space in low excitation limit, and many efficient numerical methods have been developed to solve it. (Glutsch, 2004; 1996) The macroscopic polarization in the semiconductor structure can be obtained from

$$P(t) = \frac{1}{\Omega}d^*\int d^3\mathbf{r}\psi(\mathbf{r},\mathbf{r},t), \tag{32}$$

where Ω is the normalization volume, and d^*_{cv} is the complete conjugate of the dipole matrix element d_{cv}. Some numerical results of us presented in the next section are obtained by this efficient real space approach.

4. Optical properties of semiconductor structures under external fields

An important tool in solid-state spectroscopy is the application of external fields, either static (dc) or/and dynamic (ac), electric and/or magnetic. These fields give rise to distinctive characteristic changes in the optical spectra yielding valuable information about the nature of the optical transitions. Moreover, the modulation of the optical properties of a semiconductor can be exploited for a number of advanced optoelectronic devices such as optical switches and modulators. In this section, the main characteristics in the absorption spectra of various semiconductor structures induced by external fields, particularly THz field, are reviewed.

4.1 Bulk semiconductors

The application of an external electric field will influence the relative motion of the electron-hole pair in semiconductors, which then gives rise change of the optical properties. In the case of a dc external electric field, the resulted change of optical absorption is called

Franz-Keldysh effect (FKE). (Franz, 1958; Keldysh, 1958) In Figs. 4(a) and 4(b), we show the calculated absorption spectrum without and with the excitonic effect considered. As shown in Fig. 4, pronounced oscillations above the bandgap in the absorption spectrum show up and a nonvanishing tail below the bandgap occurs. The amplitude of the oscillations decreases with increasing energy, while the oscillation period depends on the strength of the applied field. The exponential low energy absorption tail is caused by the field-induced tunneling of an electron from the valence band into the conduction band. As shown in Fig. 4(b), at high electric field, excitons are ionized, thus the results approach the free pair absorption as in Fig. 4(a).

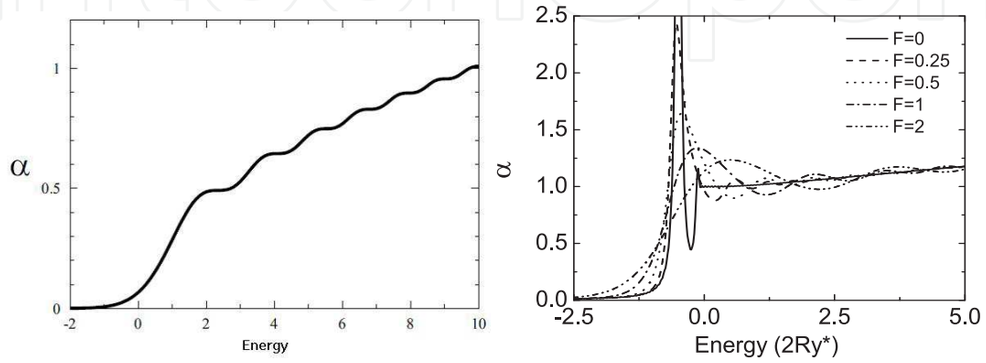

(a) (b)

Fig. 4. Franz-Keldysh effect without (a) and with excitonic effect (b). (Zhang & Zhao, 2008)

If the static electric field is replaced by a high-frequency electric field, the resulted effect is called dynamical FKE (DFKE), which was investigated by Yacoby (Yacoby, 1968) and recently by Johnsen and Jauho (Jauho & Johnsen, 1996; Johnsen & Jauho, 1998; 1999). The ac electric field modifys of the density of states both below and above the zero-field absorption threshold as shown in Fig. 5(a), and gives rise rich features in the excitonic absortion spectrum as shown in Fig. 5(b). These features are due to the replicas and THz sidebands of exciton states.

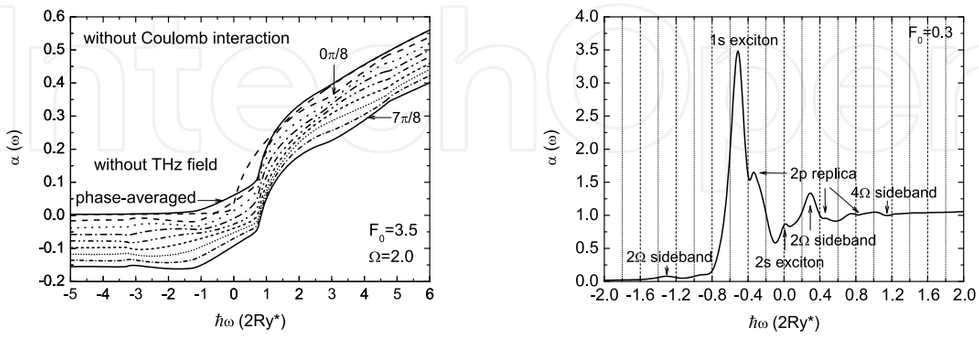

(a) (b)

Fig. 5. Density of states under THz field with different field strengthes (a) frequencies (b). (Zhang & Zhao, 2008)

Figure 6 (a) and 6(b) show the case of a THz field and a magnetic field applied to bulk semiconductor in Voigt configuration. (Zhang & Zhao, 2008) The magnetic field is $B = 4$ and $B = 2$, respectively, and the frequency of the THz field $\Omega = 2$. In both panels, the traces, from bottom to top, correspond to the THz field strength 0 to 3 at a step of 0.6. F, B, and $\Omega = 2$ are in units of excitonic energy. In the absence of the THz field (i.e. $F_0 = 0$), optical absorption spectrum exhibits a series of nearly equidistant magnetoexciton peaks, with the distance being the cyclotron frequency (B in our used units). These discrete magnetoexciton peaks stem from the Landau quantization of the orbits in the plane perpendicular to the magnetic field. The magnetoexciton resonance belonging to the lowest order Landau level shows Lorentzian lineshape, whereas the magnetoexciton resonances belonging to the higher order Landau levels show distinct Fano lineshapes. The Fano lineshapes originate from the coupling of discrete higher-order magnetoexcitons to the one-dimensional continua belonging to the lower-order Landau levels. In the presence of a strong driving THz field, the profile of the lowest magnetoexciton resonance evolves from the Lorentzian lineshape into the Fano lineshape. This change of the profile of the lowest magnetoexciton peak can be understood in the dressed states picture, i.e. the lowest magnetoexciton becomes degenerate with the continua of the lower THz-dressed magnetoexciton states. In the high frequency ($\Omega = 2$) region, the height of the lowest magnetoexcitonic resonance decreases and its width broadens. More remarkable, 2p replicas of the corresponding dark 2p magnetoexcitons of different order Landau levels show up in the continua between original magnetoexcitons. The two-THz-photon sidebands of the 1s and 2s magnetoexcitons, as well as of the 2p replica, can be identified below the lowest magnetoexciton peak and its 2p replica. Furthermore, even the two-THz-photon sideband of the 1s magnetoexciton belonging to the next neighboring higher order Landau levels can be identified. Because of the DFKE, the locations of the different magnetoexciton resonances, as well as the replicas and sidebands, blueshift to the higher energy (in addition to the diamagnetically shift).

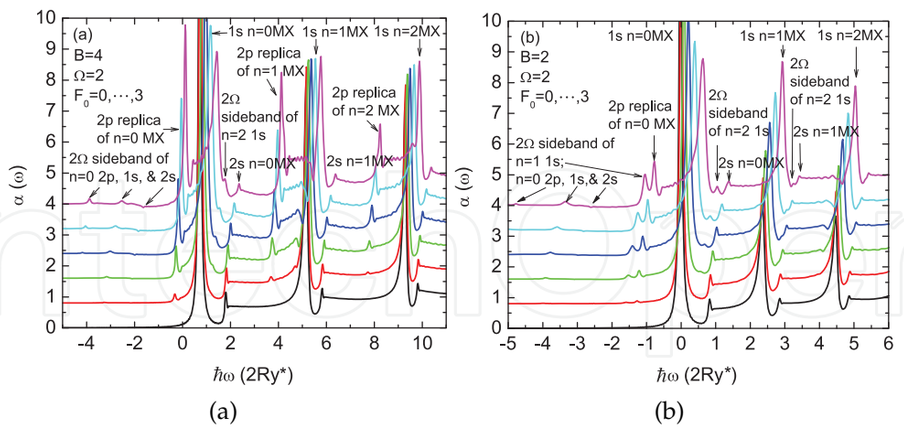

Fig. 6. (Color online) Magnetoexcitonic optical absorption spectrum of a THz-field-driven bulk GaAs in Voigt configuration. The magnetic field B=4 (a) and B= 2 (b), the frequency of the THz field $\Omega = 2$ for both case. The field strength increases from 0 to 3 from bottom to top at steps of 0.6. The index n labels the Landau levels, and MX refers to magnetoexciton. (Zhang & Zhao, 2008)

4.2 Quantum wells

Due to the quantum-confined motion of carriers in quantum wells, the excitonic and external field effects are more pronounced in semiconductor quantum wells. The spatial confinement in a quantum well prevents field ionization of the exciton up to very large field strengths. As a consequence, one can observe very large Stark shifts of exciton resonances in a field along the growth direction of the quantum well, quantum confined Stark effect (QCSE). (Miller et al., 1984; 1985)

The optical absorption of a quantum well under a growth-direction THz field was investigated by Maslov and Citrin both in SBEs approach (Maslov & Citrin, 2001) and coherent wave approach. Maslov & Citrin (2002) The main features are shown in Fig. 7. While a dc field leads to the Stark shift of excitonic peaks (QCSE) and gives rise to additional corresponding to transitions with different subband index for conduction and valence bands as in Fig. 7(a), a THz field leads to replicas around the main excitonic peak in addition to redshift and height decrease shown in Fig.7(b). Figure 7(c) shows the optical absorption with F_{dc}=50 kV/cm and different amplitudes of the THz field F_{ac} for a fixed value of the THz frequency. The excitonic peak decreases and multiple replicas appear as the THz field gets stronger. Figure 7(d) shows similar results as Fig. 7(c) but for a fixed THz field amplitude and different frequencies. For a 2 meV low-frequency THz field, the central peak is absent and only two replicas exist. If the THz frequency increases, a central peak appears and the replicas move away from the central peak. In addition to static and THz electric fields, if a magnetic field is simultaneously applied along the growth-direction of the quantum well, much richer features will show up in the absorption spectra. (Zhang & Cao, 2004)

The case in which the driving THz field polarized in the plane of quantum well was investigated by a number of authors, (Cerne et al., 1996; Jauho & Johnsen, 1996; Johnsen & Jauho, 1998; Nordstrom et al., 1998; Zhang et al., 2007) even in the presence of a magnetic field along the growth-direction. (Citrin & Hughes, 2000) It shows the following important features: (i) the main absorption edge moves to higher energies with increasing field strength, the bandedge blueshift by the ponderomotive energy, $E_{pon} = \frac{e^2F_0^2}{4m\Omega^2}$, i.e., the average kinetic energy of a particle of mass m and charge e in an electric field $F_0 \cos \Omega t$, and thus show above-band-gap transparency and increased absorption below the gap; (ii) there is a significant enhancement at the absorption edge; and (iii) the range of energies where the edge is modified increases with increasing field strengths. Figure 8 shows the experimental transmission of MQW near e1h1 exciton with $\hbar\omega_{THz} = 2.5$ meV (a) and $\hbar\omega_{THz} = 14$ meV (b) at $I_{THz} = 0, 1, 2, 4, 12$ (arbitrary units). Arrows connect calculated centers of experimental peaks and point in the direction of increasing I_{THz}. The experimental findings for the absorption are as follows (Nordstrom et al., 1998): the oscillator strength of the main absorption peak the 1s resonance is decreased by about 10-20% in the presence of the THz irradiation. There are two distinct regimes of experimental behavior as a function of THz frequency. When ω_{THz} is less than $\omega_{1s\rightarrow 2p}$, a redshift of the exciton for low THz intensities, i.e., an ac Stark shift. As THz intensity increases, this shift reaches a maximum and reverses, eventually becoming a net blueshift at the highest THz intensity; the DFKE blueshift dominates at high intensities as the ac Stark effect saturates (Fig. 8a). Conversely, if ω_{THz} is greater than $\omega_{1s\rightarrow 2p}$, a blueshift of the exciton which increases monotonically with increasing THz intensity; the ac Stark effect and DFKE act in concert, each contributing to the blueshift (Fig. 8b). In both cases, the exciton peak is broadened and suppressed, and the broadening increases with increased THz intensity.

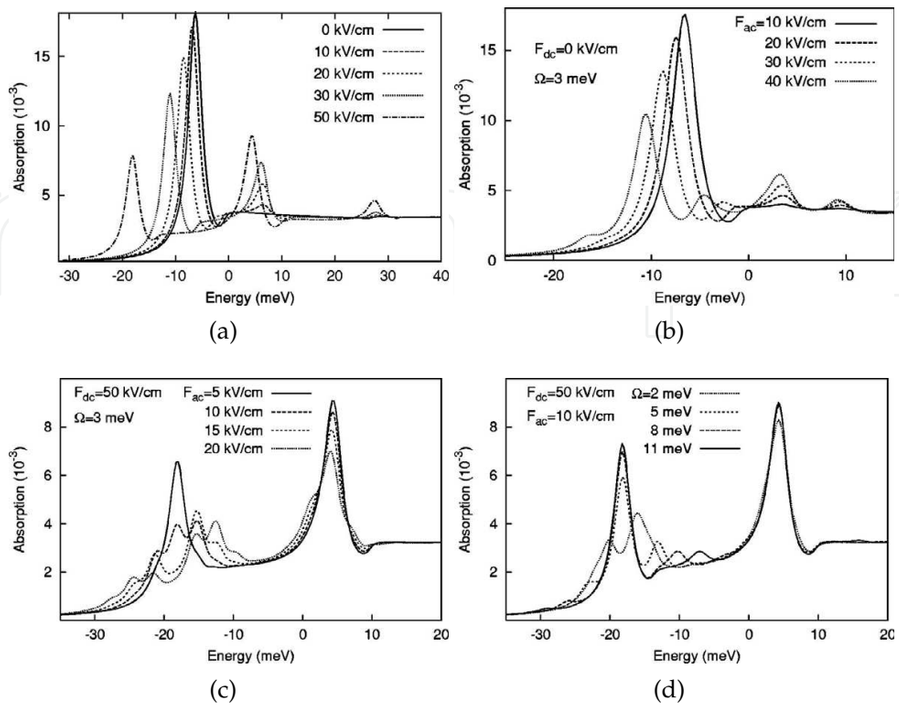

Fig. 7. Optical absorption including excitonic effects for (a) F_{dc}=0,10,20,30,50 kV/cm; (b) F_{dc}=0 kV/cm , $\hbar\Omega_{THz}$ =3 meV, and F_{ac}=10,20,30,40 kV/cm; (c) F_{dc}=50 kV/cm, $\hbar\Omega_{THz}$ =3 meV and F_{ac}=5,10,15,20 kV/cm; (d) F_{dc}=50 kV/cm, F_{ac}=10 kV/cm and $\hbar\Omega_{THz}$ =2,5,8,11 meV. (Maslov & Citrin, 2001)

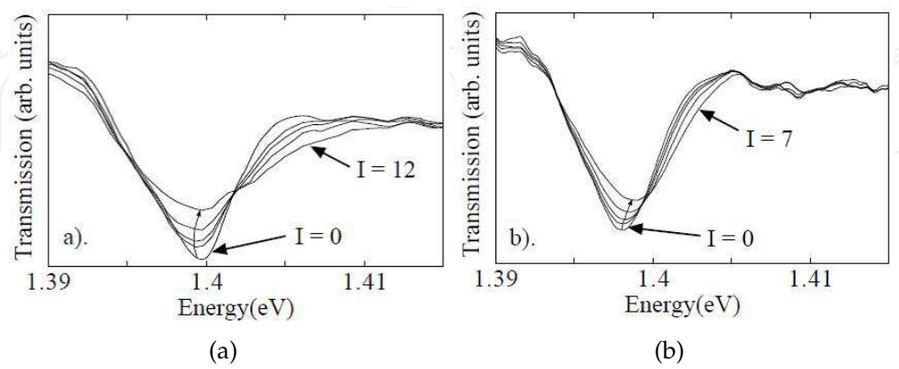

Fig. 8. Experimental transmission of MQW near e1h1 exciton. (a) $\omega_{THz} < \omega_{1s\rightarrow 2p}$, (b) $\omega_{THz} > \omega_{1s\rightarrow 2p}$. (Nordstrom et al., 1998)

The experimental features are firstly interpreted theoretically by Johnsen et al. (Nordstrom et al., 1998) by considering the interplay of DFKE and ac Stark effect in a quantum well exciton. Figiure 9 shows the calculated absorption of MQW with (a) $\hbar\omega_{THz}$ =2.5 meV<$\hbar\omega_{12}$ from top down at $\gamma = \frac{E_{pon}}{\hbar\omega_{THz}}$ =0, 0.03, 0.06, 0.1, 0.5, and 1.5. (b) $\hbar\omega_{THz}$ =14 meV>$\hbar\omega_{12}$ from top down at γ =0, 0.01, 0.02, 0.04, 0.08, and 0.15. They showed that a blue-shift of the 1s resonance if $\omega_{THz} > \omega_{1s\to 2p}$ and in a red-shift if $\omega_{THz} < \omega_{1s\to 2p}$. However as the intensity of the THz is increased the redshift saturates turns around and eventually becomes a net blue-shift.

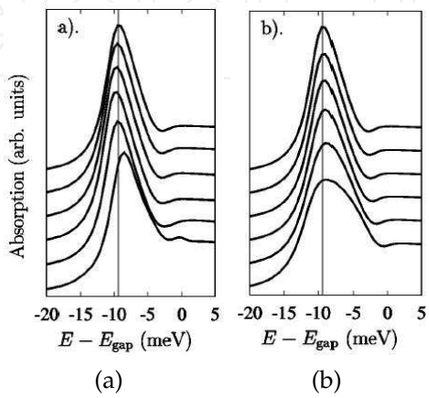

Fig. 9. Calculated absorption of MQW. (a)$\hbar\omega_{THz}$ =2.5 meV<$\hbar\omega_{12}$, (b) $\hbar\omega_{THz}$ =14 meV>$\hbar\omega_{12}$. (Nordstrom et al., 1998)

4.3 Quantum wires

Semiconductor quantum wires offer a playground for investigating the kinetics of electrons and holes in one-dimensional structures. A unique feature of the one-dimensional system is the inverse-square-root divergence of the joint density of states at the band edge. However, the Coulomb interactions between electrons and holes removes this divergence, and reduces the Sommerfield factor in contrast to the two-dimensional and three-dimensional cases. Consequently, the singular one-dimensional joint density of states does not show up at all in the linear absorption spectrum.

We have numerically analyzed the optical absorption spectra of a cylindrical quantum wire under a THz field along the axis of the wire. The cylindrical quantum wire was assumed 4200 nm in length with radius 4.2 nm. The potential at the lateral wall of the thin nanowire is assumed to be infinite, which implies the Bessel function of zero order for the envelope of the lateral ground state wave function. Considering the fundamental electron and hole subbands only, the quasi 1-D Coulomb interaction $V_{Coul}(z_e - z_h)$ is obtained from the average of the 3-D Coulomb interaction with the lateral ground state (Zhang & Zhao, 2006)

$$V_{Coul}(z_e - z_h) = \kappa \int_0^R \int_0^R \int_0^{2\pi} \int_0^{2\pi} \frac{\rho_e \rho_h J_0^2\left(\frac{\alpha_0 \rho_e}{R}\right) J_0^2\left(\frac{\alpha_0 \rho_h}{R}\right)}{\sqrt{(z_h - z_e)^2 + \rho_e^2 + \rho_h^2 - 2\rho_e \rho_h \cos(\theta_h - \theta_e)}} d\rho_e d\rho_h d\theta_e d\theta_h \tag{33}$$

where $\kappa = e^2/[4\pi^3 \varepsilon R^4 J_1^4(\alpha_0)]$, ε the dielectric constant, R the radius of the nanowire, $\theta_{e(h)}$ and $\rho_{e(h)}$ are the polar angle and radial coordinate of electron (hole) respectively, J_0, J_1 the Bessel functions and α_0 is the zero of the J_0.

The optical absorption spectra is shown in Fig. 10(a). The frequency of the THz field is 5 THz, nearly resonant with the 1s exciton in the wire. With the field strength increasing, the main exciton peak splits, and the two peaks separate farther, and broaden, even become a band, and other peaks and oscillations emerge gradually. When field strength is lower (higher) than 9 kV/cm, the peak at high (low) energy side is dominant over the one at low (high) energy side. Furthermore, the 2s resonance and the band-edge blueshift due to dynamical FK effect. There appear two-photon replica in the continuum. With the THz field increasing, the two-photon replica redshift initially and turns into blueshift and broadens. This is because the ac-Stark effect and DFKE oppose each other. In very high field, the continuum becomes oscillating, and some other peaks corresponding to multi-photon replicas occur.

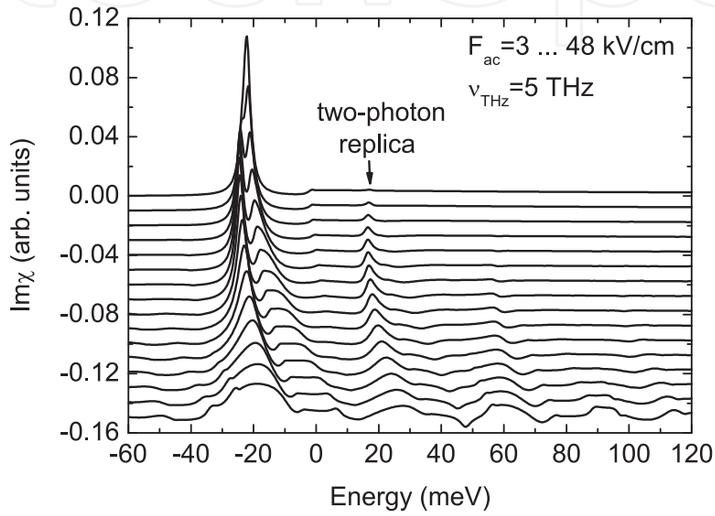

Fig. 10. (Color online) Optical absorption spectra of the cylindrical quantum wire under THz electric fields. The field strength F_{ac} varies from 3 to 48 kV/cm at the step of 3 kV/cm from top to bottom with frequency ν_{THz} of the THz field fixed at 5 THz. (Zhang & Zhao, 2006)

Figure 11 shows the spatiotemporal evolution of the polarization wave-packet for some different values of the THz field strength. The polarization wave-packet is distorted by the field and spreads to two directions following the alternating changing of the field. And there is a sharp drop for high field strength which indicates the ionization of the excitons immediately after they are generated.

The dependence of optical absorption spectra in the cylindrical quantum wire on the phase and frequency of the THz field are shown in Figs. 12(a) and 12(b). Figure 12(a) shows the influence of the frequency of the THz field on the main exciton peak. Note that the location of the dip in the splitted main 1s peak is one THz photon energy below the band-edge. Thus, this splitting is a single THz photon resonance induced coherent phenomenon. The separation and relative intensity are dependent on the frequency of THz field. Multi-photon replicas can be also identified. Figure 12(b) shows the dependence of the absorption spectra on the phase φ of the THz field at the time when the probe optical pulse reaches is peak value. The four panels show the optical absorption spectra at the frequency ν_{THz} =5 THz and the field strength F_{ac}=9 kV/cm with different phases of $\varphi = 0$, $\pi/2$, π, and $3\pi/2$, respectively. The peak emerging in the absorption continuum is the two-photon replica which is $2h\nu_{THz}$ above the 1s excitonic resonance. By changing this phase, the absorption can be enhanced or reduced at the location of the two-photon replica.

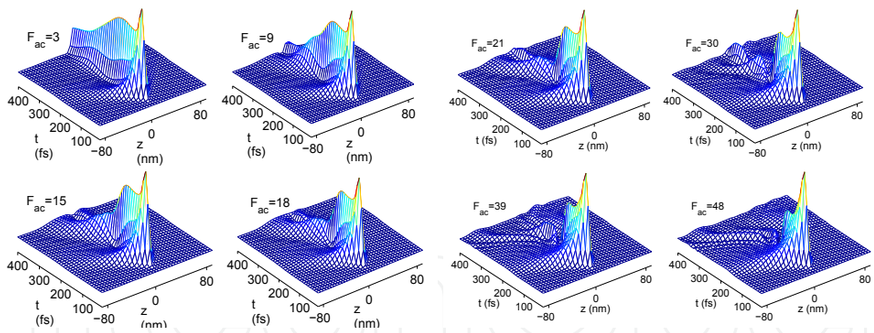

Fig. 11. (Color online) The spatiotemporal evolution of the polarization wave-packet when increasing the field strength with frequency ν_{THz}=5 THz. The eight panels correspond to different field strengths F_{ac}=3, 9, 15, 18, 21, 30, 39, and 48 kV/cm, respectively. (Zhang & Zhao, 2006)

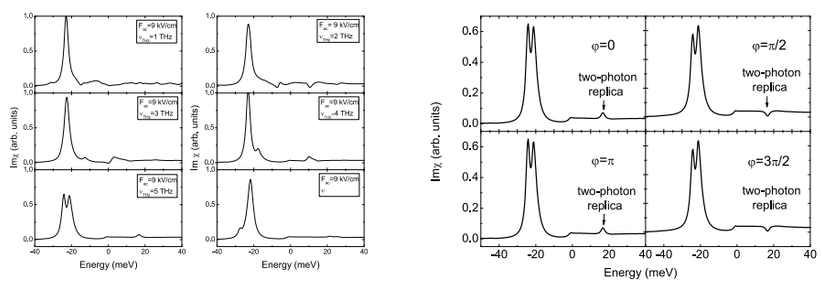

(a) (b)

Fig. 12. (a) Optical absorption spectra of the cylindrical quantum wire under THz electric fields at different frequency THz=1, 2, 3, 4, 5, and 6 THz with field strength fixed at 9 kV/cm, respectively. (b) Dependence of the optical absorption spectra of the cylindrical quantum wire on the phase under THz electric fields F_{ac}=9 kV/cm and ν_{THz}=5 THz. The four panels of b correspond to =0, $\pi/2$, π, and $3\pi/2$, respectively, with the phase of the THz wave at the time corresponding to the peak of the optical pulse. (Zhang & Zhao, 2006)

4.4 Quantum rings

Semiconductor quantum rings have been fabricated by self-organized Stranski-Krastanov growth. (Lorke et al., 2003) The not-simply-connected geometry makes them particularly interesting for studies in magnetic fields. Because the quantization of magnetic flux in the interior leads to a periodic change in the quantum mechanical properties of the electron system encircling the ring. And these periodic oscillations in the applied magnetic field are commonly called Aharonov-Bohm oscillations. This in turn affects all electronic and optical properties of rings.

Exciton absorption on a ring threaded by a magnetic flux was studied theoretically by Römer and Raikh, (Romer & Raikh, 2000) and by Hu et al. (Hu et al., 2001) Electronic structure of a quantum ring in a lateral electric field was studied theoretically by Llorens et al. (Llorens et al., 2001), and they show that the energy levels of large quantum rings exhibit a complex dispersion as a function of the electric field due to the break of axial symmetry by the field. The electric field effect on the Bohm-Aharonov oscillations is investigated by Barticevic.

(Barticevic et al., 2002) And Enhancement of the Aharonov-Bohm effect of excitons with a lateral static electric field is shown by Maslov and Citrin. (Maslov & Citrin, 2003)
We have investigated the effect of a lateral THz electric field on the excitonic AB effect using real space appraoch. (Zhang et al., 2005) Figure 13 shows the optical absorption in a nanoring with radius 50 nm under a lateral ac field and different magnetic flux Φ through the ring. The photon energy of the ac electric field in Figs. 13(a) and 13(b) is 0.256 meV and 10.22 meV, respectively, but with the same strength 5 kV/cm. We see that the shape of the exciton peak does not change noticeable with magnetic flux in the lower frequency ac field, but there is a slightly blue shift of the exciton peak with the flux increasing. However, in the higher frequency ac field, the exciton peak splits remarkably and a prominent peak appears bellow the main exciton peak, which is the replica of the dark exciton state just below the bandgap.

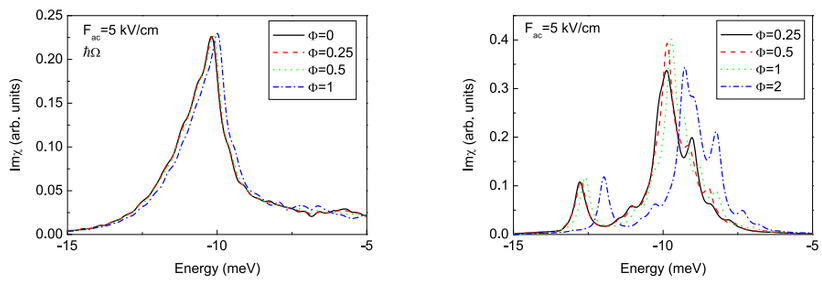

(a) (b)

Fig. 13. (Color online) Optical absorption of the nanoring under a lateral THz field and a perpendicular magnetic field. (a) In the presence of a lateral THz field with $F_{ac} = 5$ kV/cm and $\hbar\Omega = 0.256$ meV, and different magnetic flux. (b) In the presence of the lateral THz field with $F = 5$ kV/cm and $\hbar\Omega = 10.22$ meV, and different magnetic flux. (Zhang et al., 2005)

4.5 Superlattices

Semiconductor superlattices provide insight into certain new areas of solid-state physics which cannot be accessed in conventional crystals, such as Bloch oscillation and dynamical localization. The observation of the Wannier-Stark ladder (WSL) in optical-absorption spectra of semiconductor superlattices ended a long-lasting debate about the formation of quasidiscrete energy levels when a strong dc electric field F is applied to an insulating crystal. In the absorption spectra a corresponding series of equidistant transitions with quasi-two-dimensional character show up. It is strikingly different from the FKE. Howevwer, the FKE was also expected to be obtained for low fields. The coexistence of both WSL and FKE in the same structure was demonstrated and a consistent explanation of both effects was given by Linder et al, (Linder, 1997) showing that the FKE basically consists of an intensity modulation of the WSL transitions.
Figure 14(a) shows calculated excitonic absorption spectra over a wide range of the electric field for a narrow-miniband superlattice. The narrow-miniband system is between the quasi-2D and the 3D wide-band limit of bulk material. The corresponding spectra without the Coulomb interaction shown in (b) for comparison. At high fields WS transitions can clearly be resolved as excitonic peaks in (a). For decreasing field, the energetic distance between the WS transitions falls below the value of the broadening parameter and individual peaks can

no longer be resolved. Gradually, the structures in the spectra transform to a pattern which is characteristic for FK oscillations in low fields.

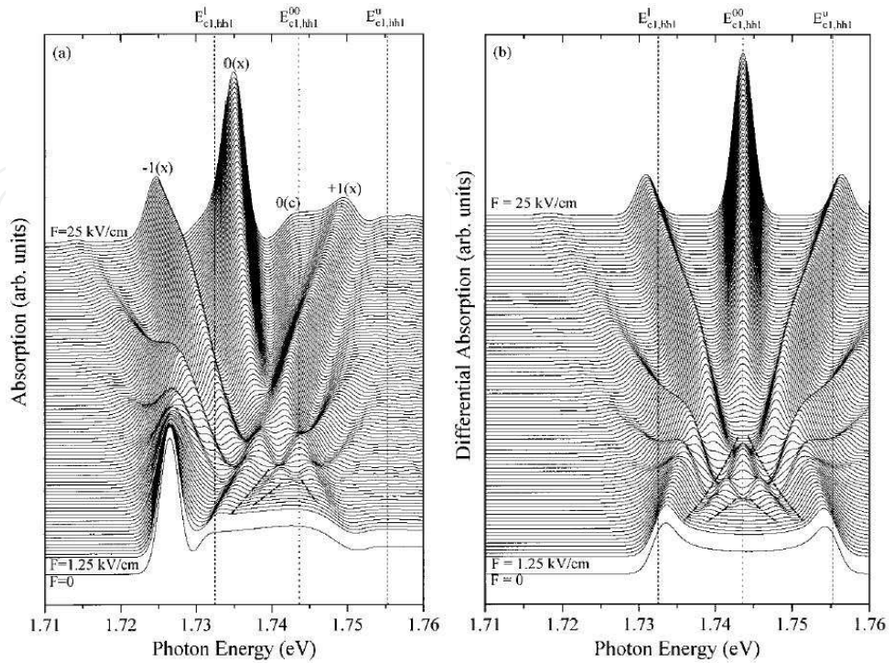

Fig. 14. Excitonic absorption spectra over a wide range of the electric field for a narrow-miniband superlattice. (a) calculated with excitonic effect, (b) calculated without excitonic effect (Linder, 1997)

Figure 15 shows excitonic absorption spectra over a wide range of the electric field for a wide-miniband superlattice. In this case, the superlattice is closer to a 3D system. Figure 15(a) shows the experimental absorption spectra, and Fig. 15(b) and (c) shows the calculated results with and without excitonic effect considered. The theoretical results agree very well with the experimental results.

The optical absorption spectra of semiconductor superlattices under a combined dc-ac fields, $F_{dc} + F_{ac} \cos v_L t$, is also calculated based on SBEs. (Je et al., 2001; Zhang et al., 2003) Figure 16(a) shows the absorption spectra of a superlattice under a dc field ($eF_{dc}d$=20 meV) without applied ac field and those under an ac field ($f \equiv eF_{ac}d/\hbar\omega_L$=3.83 and $\hbar\omega_L$ =10 meV) without applied dc field. The dc field has sufficient strength to provide WSL's. The four dominant peaks correspond to WSL with $m = 0$, $m = -1$, $m = -2$, and $m = 1$, respectively. The Coulomb interactions result in smaller ladder spacing than the value of Bloch frequency. The WSL peak with $m = 1$ is largely broadened and much weaker than the WSL peak with $m = -1$, since they exist in the ionization-continuum of negative WSL states. The absorption spectra under the ac field have an exciton peak at 1.578 eV ($m' = 0$) and its second eigen state at 1.569 eV ($m' = -1$). Another peaks at 1.559 eV ($m' = -2$), 1.55 eV ($m' = -3$), and 1.54 eV ($m' = -4$) correspond to dynamical Stark ladders (DSL's) caused by the ac field. The ladder spacing estimated from these DSL's is almost $\hbar\omega_L$. Figure 16(b) displays the absorption spectra under the ac fields with different strengths f and the dc field of a fixed

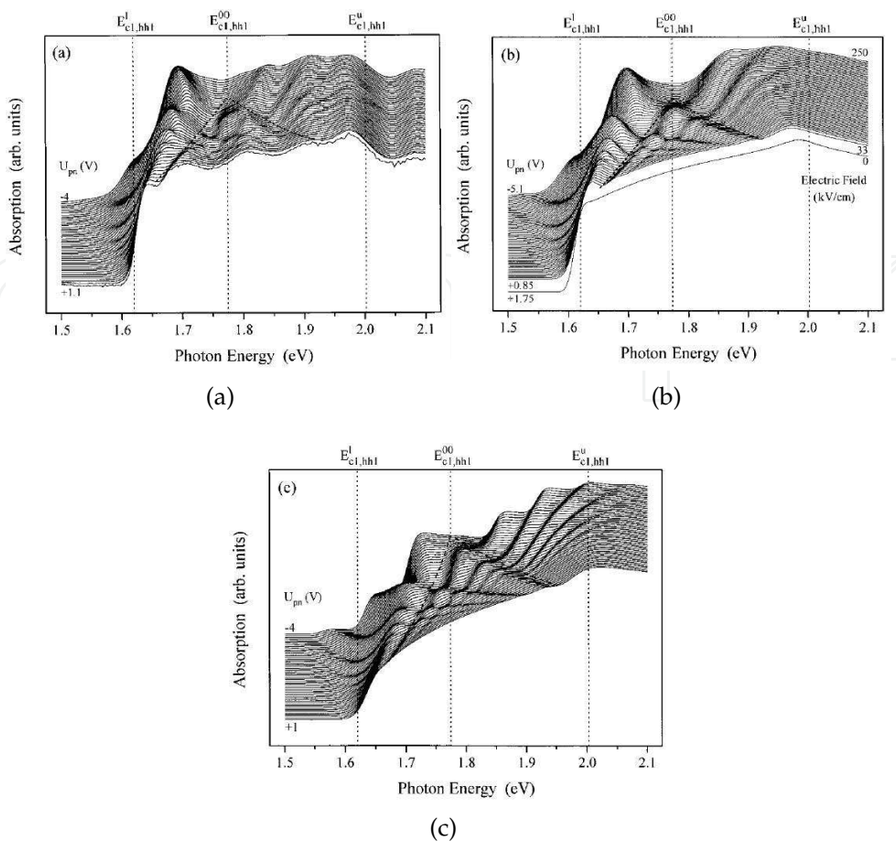

Fig. 15. Excitonic absorption spectra over a wide range of the electric field for a wide-miniband superlattice. (a) experimental,(b) calculated with excitonic effect, (c) calculated without excitonic effect. (Linder, 1997)

strength $eF_{dc}d = 20$ meV. A peak at 1.577 eV corresponds the WSL with the index $m = 0$. As the strength of the ac field increases, the DSL's appear with the same spacing energy $\hbar\omega_L$. The DFSL's between WSL's positions are also observed. Nearly all of the peaks, corresponding to the spectral positions at the formula $\epsilon_0 + m\hbar\omega_B + m\prime\hbar\omega_L$, exist. Almost all the peaks can be identified by (m, m').

4.6 Quantum-dot-superlattices

Recently, a structure consisting of a series of quantum dots interlaced along a nanowire has been grown. This quantum dot superlattice structure has characteristics of quantum dots, quantum wires and superlattices. As the band offset of different materials confines the carriers in one of the quantum dots, the electron states have zero-dimensional (0D) characteristics of a quantum dot. However, by tunneling between adjacent quantum dots the carriers can travel along the wire axis. Thus, a miniband electronic structure of an superlattice is formed. Due to strong lateral confinement, the carrier motion in the plane perpendicular to the wire axis is confined so that the system has characteristics of one-dimensional structures.

The effects of an external THz field applied along the quantum-dot-superlattice nanowire on the interband optical absorption spectra are shown in Fig. 17. Figure 17(a) shows

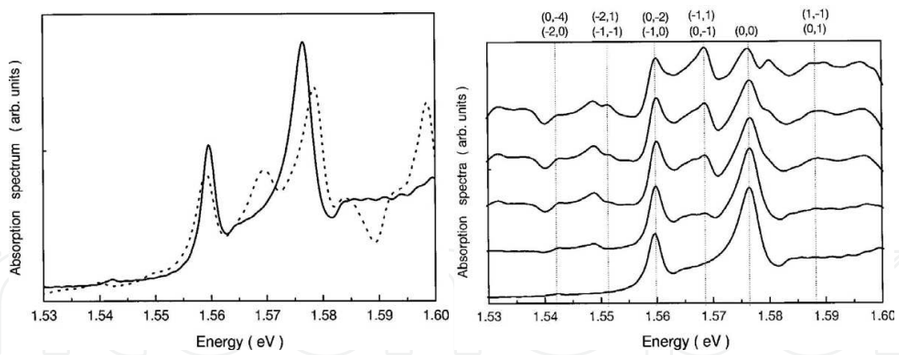

(a) (b)

Fig. 16. (a) The absorption spectra for $eF_{dc}d$=20 meV and f=0 (solid line) and F_{dc}=0 and f=2.83 with $\hbar\omega_L$ =10 meV (dotted line). (b) Absorption spectra under the combined dc-ac fields when $eF_{dc}d$=20 meV and $\hbar\omega_L$ = 10 meV. The spectra are shown for the different strengths of the ac fields or f =0, 0.2, 0.4, 0.6, 0.8, and 1 from the bottom. Indices in the upper part of the figure is (m, $m\prime$).(Je et al., 2001)

the absorption spectra for different frequencies of $\hbar\Omega$=5, 11, and 20 meV of the THz field, respectively, with the field strength fixed at F_{ac} = 30 kV/cm. The main exciton peak decreases, broadens and becomes asymmetric due to the applied THz field. It has small gain and small peaks appears in the spectra. These peaks are replicas and THz-sideband of the excitonic states dressed by THz photons. The excitonic absorption spectra for different field strengths F_{ac} with frequency fixed at $\hbar\Omega$=20 meV are shown in Fig. 17(b). The oscillator strength is completely transferred from the minibands to the exciton. Increasing field strength the main excitonic peak decreases, broadens and splits up. The asymmetric splitting resemble the well known Autler-Townes splitting of atoms in an ac driving field and is due to the coherent coupling of the lowest and higher exciton states. Furthermore, when the field strength increase, there exists one-photon and two-photon gain in the optical spectra.

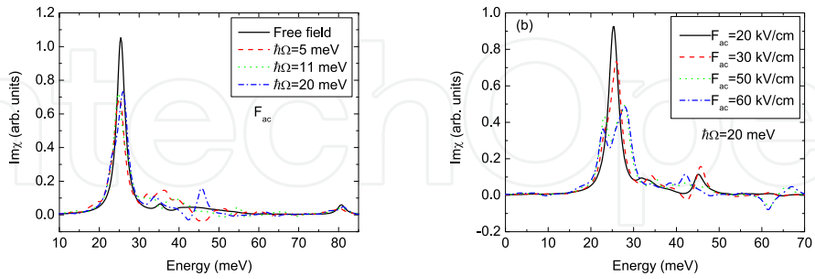

(a) (b)

Fig. 17. (Color online) Optical absorption in the QDSLW under a THz field F_{ac} along the wire. (a) Different frequencies $\hbar\Omega$=5, 11, and 20 meV, with field strength fixed at F_{ac}=30 kV/cm; (b) Different field strengths F_{ac}=20, 30, 50, and 60 kV/cm, with frequency fixed at $\hbar\Omega$=20 meV. (Zhang et al., 2005)

4.7 Microcavities

As semiconductor fabrication technology developed, it became possible to fabricate high-quality-factor (high-Q) semiconductor microcavities. In a system of quantum wells embedded within high-Q semiconductor microcavity, the strong exciton-photon coupling leads to the formation of two new eigenstates of the exciton-photon coupled system, called "microcavity exciton polariton" states. Thus results in two spectroscopically pronounced exciton polariton peaks in the absorption spectrum of the system. In a high-Q microcavity, most of the photons arising from the interband polarization associated with one exciton internal state are fed back into the system. This leads to a photon-mediated radiative renormalization of the optically allowed (i.e., s-like) exciton internal states. As shown in the subsection 4.2, a quantum well in the simultaneous presence of a THz field polarized in the growth direction and an incident optical field near an excitonic resonance results in substantial frequency mixing between the THz and optical fields, and leads to THz-sideband generation. In a high-Q optical microcavity, THz-sideband generation is strongly enhanced. Numerical estimate by Citrin (Citrin, 2002) showed that the values of the reflected intensity into the first THz sideband can be as large as 10% of the reflected intensity at the fundamental, and a factor of ~100 enhancement of doubly resonant THz-sideband generation in the microcavity compared with bare quantum well. In Fig. 18(a), the optical frequency dependence of the reflected field (solid) and the interband polarization (dashed) in the first THz sideband in a high-Q microcavity are shown. The frequency dependence of the reflected field in the fundamental from the same structure is shown in Fig. 18(b). The curves are normalized to the incident field amplitude.

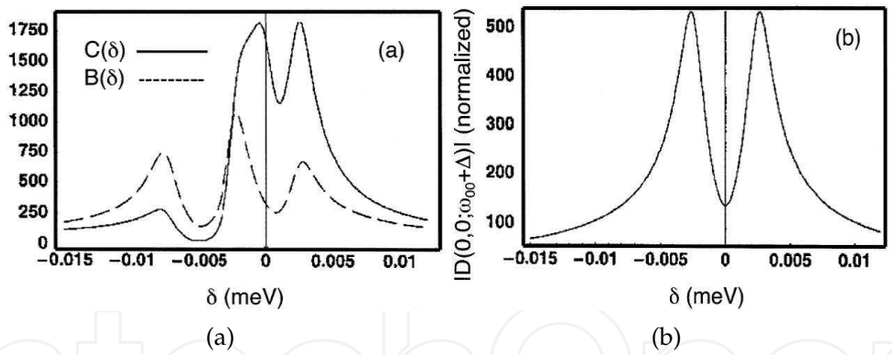

Fig. 18. (a) Optical frequency dependence of the reflected field (solid) and the interband polarization (dashed) in the first THz sideband in a high-quality-factor microcavity. (b) The frequency dependence of the reflected field in the fundamental from the same structure. The curves are normalized to the incident field amplitude. (Citrin, 2002)

Citrin (Citrin, 1999) also showed that ultrafast THz pulse can be used to control coherently the NMOs in microcavities. He showed that a THz pulse can introduce a phase shift, amplitude modulation, or both in the optical dynamics depending on whether the induced modulation is real, imaginary, or complex. Thus, by judiciously choosing the THz pulse, it is possible in principle to switch the coherent emission from a microcavity undergoing mode oscillations to emit at either norm mode following the incidence of the THz pulse. This is shown in Fig. 19. Fig. 19(a) shows the unmodulated signal. In (b), for $t < 0$, the emission occurs at the upper mode. Fig. 19(c) shows that the phase of the mode oscillations has been flipped at $t = 0$. And

Fig. 19(d) shows the case where the coherent emission for $t > 0$ is effectively quenched due to the modulation of the exciton linewidth by a THz pulse.

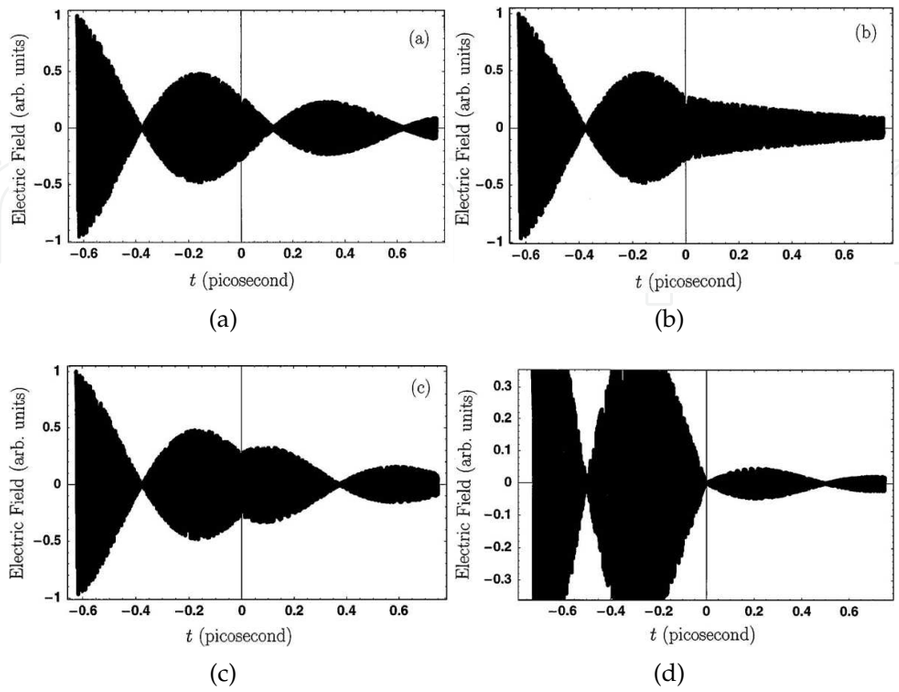

Fig. 19. Electric field in MC following ultrafast broad-band optical excitation. (a) The unmodulated case. (b) A THz pulse is used to shift the emission to the upper norm mode ε_+ at t=0. (c) Shows how a THz pulse can be used to invert the dynamics of the mode oscillations. (d) By introducing transient rapid dephasing when the excitation is in the exciton mode at time t=0, the coherent emission is quenched.

5. Conclusion

To summary, we have reviewed the generation of THz pulses by using femtosecond laser pulses to excite photoconductive antennas, nonlinear optical crystals, and quantum-confined semiconductor structures. THz radiation is emitted from these materials via transient photocurrent, optical rectification, and beat of a coherent superposition of different states, respectively. Then we present the fundamental formulism and the powerful extended SBEs used to calculate the macroscopic polarization and absorption coefficient in various semiconductor structures. The SBEs is presented in *k*-space and in real-space, respectively. We have applied these formulation to deal with the optical absorption in various different semiconductor structures driven by a strong THz electric field. The investigated objects involved bulk and quantum-confined semiconductor structures, such as quantum wells, quantum wires, quantum rings, superlattices, quantum-dot-superlattices, etc. Many fascinating phenomena, such as dynamical Franz-Keldysh effect, ac Stark effect, THz-sideband generation, replicas of resonant excitonic peaks, show up in the optical spectra of these structures in the simultaneous presence of a strong pumping THz field and a probing

infrared pulse. These effects may be employed to develop advanced optoelectronic and THz devices.

6. Acknowledgments

This work is supported by the National Basic Research Program of China (973 Program) (2007CB310405) and the National Natural Science Foundation of China (10834015 and 60777017). The authors also gratefully acknowledge the support of K. C. Wong Education Foundation, Hong Kong.

7. References

Barticevic, Z.; Fuster, G. &Pacheco, M. (2002). Effect of an electric field on the Bohm-Aharonov oscillations in the electronic spectrum of a quantum ring. *Phys. Rev. B*, Vol.65(No.19): 193307-1-4

Binder, E.; Kuhn, T. &Mahler, G. (1994). Coherent intraband and interband dynamics in double quantum wells: Exciton and free-carrier effects. *Phys. Rev. B*, Vol.50(No.24): 18319-18329.

Černe, J.; Kono, J.; Sherwin, M. S.; Sundaram, M.; Gossard, A. C. &Bauer, G. E.W. (1996). Terahertz dynamics of excitons in GaAsyAlGaAs quantum wells. *Phys. Rev. Lett.*, Vol.77(No.6): 1131-1134.

Citrin, D. S. (1999). Terahertz sideband generation and coherent control in semiconductor microcavities. *Phys. Rev. Lett.*, Vol.82(No.15): 3172-3175.

Citrin, D. S. &Hughes, S. (2000). Franz-Keldysh effect on Landau levels and magnetoexcitons in quantum wells. *Phys. Rev. B*, Vol.61(No.8): R5105-R5108.

Citrin, D. S. (2002). Terahertz/optical mixing in symmetric semiconductor quantum wells embedded in optical microcavities. *J. Lightwave Technology*, Vol.20(No.12): 1983-1988.

Darrow, J. T.; Zhang, X. -C.; Auston, D. H. &Morses, J. D. (1992). Saturation properties of large-aperture photoconducting antennas. *IEEE J. Quantum Electron*, Vol.28(No.6): 1607-1616.

Franz, W. Z. (1958). Einfluβ eines elektrischen Feldes auf eine optische Absorptionskante. *Naturforsch*, Vol.13a 484-489.

Glutsch, S. (2004). *Excitons in Low-Dimensional Semiconductors*, Springer, Berlin.

Glutsch, S.; Chemla, D. S. &Bechstedt, F. (1996). Numerical calculation of the optical absorption in semiconductor quantum structures. *Phys. Rev. B*, Vol.54(No.16): 11592-11601.

Haug, H. &Koch, S. W. (2004). *Quantum Theory of the Optical and Electronic Properties of Semiconductors*, 4th ed., World Scientific, Singapore.

Hu, H.; Zhu, J.; Li, D. &Xiong, J. (2001). Aharonov-Bohm effect of excitons in nanorings. *Phys. Rev. B*, Vol.63(No.19): 195307-1-11.

Huber, R.; Brodschelm, A.; Tauser, F. &Leitenstorfer A. (2000). Generation and field-resolved detection of femtosecond electromagnetic pulses tunable up to 41 THz. *Appl. Phys. Lett.*, Vol.76(No.22): 3191-3193.

Jauho, A. -P. &Johnsen, K. (1996). Dynamical Franz-Keldysh effect. *Phys. Rev. Lett.*, Vol.76(No.24): 4576-4579.

Je, K.; Park, S. &Kim, Y. (2001). Optical absorption spectra and dynamical fractional Stark ladders in semiconductor superlattices. *Phys. Rev. B*, Vol.64(No.7): 075111-1-5.

Johnsen, K. &Jauho, A. -P. (1998). Linear optical absorption spectra of mesoscopic structures in intense THz fields: Free-particle properties. *Phys. Rev. B*, Vol.57(No.15): 8860-8872.

Johnsen, K. &Jauho, A. -P. (1999). Quasienergy spectroscopy of excitons. *Phys. Rev. Lett.*, Vol.83(No.6): 1207-1210.

Keldysh, L. V. (1958). The effect of a strong electric field on the optical absorption properties of insulating crystals. *Sov. Phys.-JETP*, Vol.34(No.7): 788-790. [*Zh. Eksp. Theor. Fiz.* Vol.34(No.):1138-1141.]

Linder, N. (1997). Excitons in superlattices: absorption asymmetry, dimensionality transition, and exciton localization *Phys. Rev. B*, Vol.55(No.20): 13664-13676.

Llorens, J. M.; Trallero-Giner, C.; García-Cristóbal, A. &Cantarero, A. (2001). Electronic structure of a quantum ring in a lateral electric field. *Phys. Rev. B*, Vol.64(No.3): 035309-

Lorke, A.; Garcia, J. M.; Blossey, R.; Luyken, R. J. &Petroff, P. M. (2001). Self-organized InGaAs quantum rings–fabrication and spectroscopy, *in* Kramer, B. (Ed.), *Adv. in Solid State Phys.*, Springer-Verlag, Berlin: Heidelberg, 125-137.

Maslov, A. V. &Citrin, D. S. (2001). Optical absorption of THz-field-driven and dc-biased quantum wells. *Phys. Rev. B*, Vol.64(No.15): 155309-1-10.

Maslov A. V. &Citrin, D. S. (2002). Numerical calculation of the terahertz field-induced changes in the optical absorption in quantum wells. *IEEE J. Selected Topics in Quantum Electronics*, Vol.8(No.3): 457-463.

Maslov, A. V. &Citrin, D. S. (2003). Enhancement of the Aharonov-Bohm effect of neutral excitons in semiconductor nanorings with an electric field. *Phys. Rev. B*, Vol.67(No.12): 121304-1-4.

Meier, T.; von Plessen, G.; Thomas, P. &Koch, S. (1994). Coherent electric-field effects in semiconductors. *Phys. Rev. Lett.*, Vol.73(No.6): 902-905.

Meier, T.; von Plessen, G.; Thomas, P. &Koch, S. (1995). Coherent effects induced by static and time-dependent electric fields in semiconductors. *Phys. Rev. B*, Vol.51(No.20): 14490-14497.

Meier, T.; Rossi, F.; Thomas, P. &Koch, S. (1995). Dynamic localization in anisotropic Coulomb systems: Field induced crossover of the exciton dimension. *Phys. Rev. Lett.*, Vol.75(No.13): 2558-2561.

Miller, D. A. B.; Chemla, D. S.; Damen, T. C.; Gossard, A. C.; Wiegmann, W.; Wood, T. H. &Burrus, C. A. (1984). Band-edge electroabsorption in quantum well structures: The quantum-confined Stark effect. *Phys. Rev. Lett.*, Vol.53(No.22): 2173-2176.

Miller, D. A. B.; Chemla, D. S.; Damen, T. C.; Gossard, A. C.; Wiegmann, W.; Wood, T. H. &Burrus, C. A. (1985). Electric field dependence of optical absorption near the band gap of quantum-well structures. *Phys. Rev. B*, Vol.32(No.2): 1043-1060.

Nordstrom, K. B.; Johnsen, K.; Allen, S. J.; Jauho, A.-P.; Birnir, B.; Kono, J.; Noda, T.; Akiyama, H. &Sakaki, H. (1998). Excitonic dynamical Franz-Keldysh effect. *Phys. Rev. Lett.*, Vol.81(No.2): 457-460.

Planken, P. C. M.; Nuss, M. C.; Brener, I.; Goossen, K. W.; Luo, M. S. C.; Chuang, S. L. &Pfeiffer L. (1992). Terahertz emission in single quantum wells after coherent optical excitation of light hole and heavy hole excitons. *Phys. Rev. Lett.*, Vol.69(No.26): 3800-3803.

Römer, R. A. &Raikh, M. E. (2000). Aharonov-Bohm effect for an exciton. *Phys. Rev. B*, Vol.62(No.11): 7045-7049.

Roskos, H. G.; Nuss, M. C.; Shah, J.; Leo, K.; Miller, D. A. B.; Fox, A. M.; Schmitt-Rink, S. &Köhler, K. (1992). Coherent submillimeter-wave emission from charge oscillations in a double-well potential. *Phys. Rev. Lett.*, Vol.68(No.14): 2216-2219.

Sakai, K. &Tani, M. (2005). Introduction to Terahertz Pulses, *in* Sakai, K.(Ed.), *Terahertz Optoelectronics*, Springer-Verlag, Berlin: Heidelberg, 6.

Yacoby, Y. (1968). High-frequency Franz-Keldysh effect. *Phys. Rev.*, Vol.169(No.3): 610-619.

Zhang, A.; Yang, L. &Dignam, M. M. (2003). Influence of excitonic effects on dynamic localization in semiconductor superlattices in combined dc and ac electric fields. *Phys. Rev. B*, Vol.67(No.20): 205318-1-7.

Zhang, T. Y. &Cao, J. C. (2004). Study of the surface and far fields of terahertz radiation generated by large-aperture photoconductive antennas. *Chin. Phys.*, Vol.13(No.10): 1742-1746.

Zhang, T. Y. &Cao, J. C. (2004). Optical absorption in terahertz-driven quantum wells under a magnetic field *J. Phys.: Condens. Matter*, Vol.16(No.49): 9093-9101.

Zhang, T. Y. &Cao, J. C. (2005). Optical absorption in semiconductor nanorings under a lateral terahertz electric field. *J. Appl. Phys.*, Vol.97(No.2): 024307-1-5.

Zhang, T. Y.; Zhao, W.; Cao, J. C. &Qasim, G. (2005). Interband optical-absorption spectra of a finite quantum dot superlattice in a cylindrical nanowire. *J. Appl. Phys.*, Vol.98(No.9): 094311-1-5.

Zhang, T. Y. &Zhao, W. (2006). Franz-Keldysh effect and dynamical Franz-Keldysh effect of cylindrical quantum wires. *Phys. Rev. B*, Vol.73(No.24): 245337-1-6.

Zhang, T. Y.; Zhao, W.; Liu, X. M. &Zhang, C. (2007). Nonlinear optical properties of semiconductor quantum wells under intense terahertz radiation. *Appl. Phys. Lett.*, Vol.91(No.4): 041909-1-3.

Zhang, T. Y. &Zhao, W. (2008). Excitonic optical absorption in semiconductors under intense terahertz radiation. *Chin. Phys. B* , Vol.17(No.11): 4285-4291.

Zhang, T. Y. &Zhao, W. (2008). Magnetoexcitonic optical absorption in semiconductors under strong magnetic fields and intense terahertz radiation in the Voigt configuration. *Europhys. Lett.*, Vol.82(No.6): 67001-1-6.

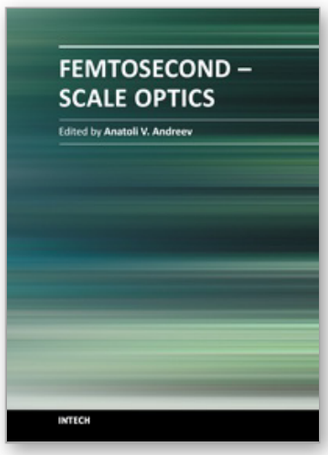

Femtosecond-Scale Optics
Edited by Prof. Anatoly Andreev

ISBN 978-953-307-769-7
Hard cover, 434 pages
Publisher InTech
Published online 14, November, 2011
Published in print edition November, 2011

With progress in ultrashort ultraintense laser technologies the peak power of a laser pulse increases year by year. These new instruments accessible to a large community of researchers revolutionized experiments in nonlinear optics because when laser pulse intensity exceeds or even approaches intra-atomic field strength the new physical picture of light-matter interaction appears. Laser radiation is efficiently transformed into fluxes of charged or neutral particles and the very wide band of electromagnetic emission (from THz up to x-rays) is observed. The traditional phenomena of nonlinear optics as harmonic generation, self-focusing, ionization, etc, demonstrate the drastically different dependency on the laser pulse intensity in contrast the well known rules. This field of researches is in rapid progress now. The presented papers provide a description of recent developments and original results obtained by authors in some specific areas of this very wide scientific field. We hope that the Volume will be of interest for those specialized in the subject of laser-matter interactions.

How to reference
In order to correctly reference this scholarly work, feel free to copy and paste the following:

Tong-Yi Zhang and Wei Zhao (2011). Optical Properties of Quantum-Confined Semiconductor Structures Driven by Strong Terahertz Fields, Femtosecond-Scale Optics, Prof. Anatoly Andreev (Ed.), ISBN: 978-953-307-769-7, InTech, Available from: http://www.intechopen.com/books/femtosecond-scale-optics/optical-properties-of-quantum-confined-semiconductor-structures-driven-by-strong-terahertz-fields

INTECH
open science | open minds

InTech Europe
University Campus STeP Ri
Slavka Krautzeka 83/A
51000 Rijeka, Croatia
Phone: +385 (51) 770 447
Fax: +385 (51) 686 166
www.intechopen.com

InTech China
Unit 405, Office Block, Hotel Equatorial Shanghai
No.65, Yan An Road (West), Shanghai, 200040, China
中国上海市延安西路65号上海国际贵都大饭店办公楼405单元
Phone: +86-21-62489820
Fax: +86-21-62489821

IntechOpen